

# SCIENTIFIC REPORTS



OPEN

## A Facile and Low-Cost Route to Heteroatom Doped Porous Carbon Derived from Broussonetia Papyrifera Bark with Excellent Supercapacitance and CO<sub>2</sub> Capture Performance

Received: 02 November 2015

Accepted: 18 February 2016

Published: 03 March 2016

Tongye Wei<sup>1</sup>, Qi Zhang<sup>1</sup>, Xiaolin Wei<sup>1</sup>, Yong Gao<sup>2</sup> & Huaming Li<sup>2</sup>

In this work, we present a facile and low-cost approach to synthesize heteroatom doped porous carbon via hydrothermal treatment of stem bark of broussonetia papyrifera (BP) as the biomass precursor in diluted sulfuric acid, and following thermal activation by KOH at 800 °C. The morphology, structure and textural property of the prepared porous carbon (PC) are investigated by scanning electron microscopy, transmission electron microscopy, N<sub>2</sub> sorption isotherms, and X-ray photoelectron spectroscopy. The porous carbon possesses a high BET surface area of 1759 m<sup>2</sup> g<sup>-1</sup> and an average pore size of 3.11 nm as well as hetero-oxygen (9.09%) and nitrogen (1.7%) doping. Such porous carbon shows outstanding capacitive performances of 416 F g<sup>-1</sup> and 300 F g<sup>-1</sup> in three and two-electrode systems, respectively. As a solid-state adsorbent, the obtained porous carbon has an excellent CO<sub>2</sub> adsorption capacity at ambient pressures of up to 6.71 and 4.45 mmol g<sup>-1</sup> at 0 and 25 °C, respectively. The results present one novel precursor-synthesis route for facile large-scale production of high performance porous carbon for a variety of great applications including energy storage and CO<sub>2</sub> capture.

Activated carbons (ACs) have been attracting a lot of investigation in previous decades. The reason for this attention is due to it is cheap, abundant, environmentally safe, commercially available and a sustainable biological resource<sup>1</sup>. Generally, ACs are usually prepared by a two-step process, in which carbon precursors are pyrolyzed at temperatures in the range of 600 ~ 900 °C in an inert atmosphere such as Ar or N<sub>2</sub>, followed by physical activation at elevated temperature in the presence of suitable oxidizing atmosphere chemical activation process using chemical agents such as KOH, NaOH, H<sub>3</sub>PO<sub>4</sub>, and ZnCl<sub>2</sub><sup>1-4</sup>. It has been demonstrated that the incorporation of heteroatoms, such as sulfur, boron, nitrogen, and oxygen, into the carbon lattice can significantly enhance mechanical, semi-conducting, field-emission, and electrical properties of carbon materials. For example, nitrogen doping is considered to be the most promising method for enhancing surface polarity, electric conductivity and electron-donor tendency of the ACs, thereby improving their performances in CO<sub>2</sub> capture, electric double-layer capacitors, fuel cells, and catalysis<sup>5</sup>. To prepare these materials, one approach is to use nitrogen-containing original precursors<sup>6</sup> or ionic liquids<sup>7</sup> for pyrolysis, and another approach is to post-treat carbon with N-containing dopants such as ammonia, amine, or urea<sup>8</sup>. Biomass is an attractive original precursor, which is cheap, environment friendly and readily available in high quality and quantity. In addition to its carbon and water content, biomass is rich in elements such as sulfur, nitrogen, and phosphorus, as well as metals such as Fe, Cu, and others<sup>9</sup>. Up to now, however, only a small portion of biomass materials such as pig bones, egg white protein, amaranth, hemp<sup>10</sup>, bean dregs<sup>11,12</sup>, seaweeds<sup>13</sup> or seaweed biopolymers<sup>14,15</sup>, etc., are used as carbon precursors for supercapacitor electrodes and CO<sub>2</sub> capture. Therefore, the search for new precursors, which are cheap, accessible and

<sup>1</sup>Hunan Key Laboratory of Micro-Nano Energy Materials and Devices, Department of Physics, Xiangtan University, Xiangtan 411105, Hunan Province, P. R. China. <sup>2</sup>College of Chemistry, Xiangtan University, Xiangtan 411105, Hunan Province, P. R. China. Correspondence and requests for materials should be addressed to X.W. (email: xlw@xtu.edu.cn)

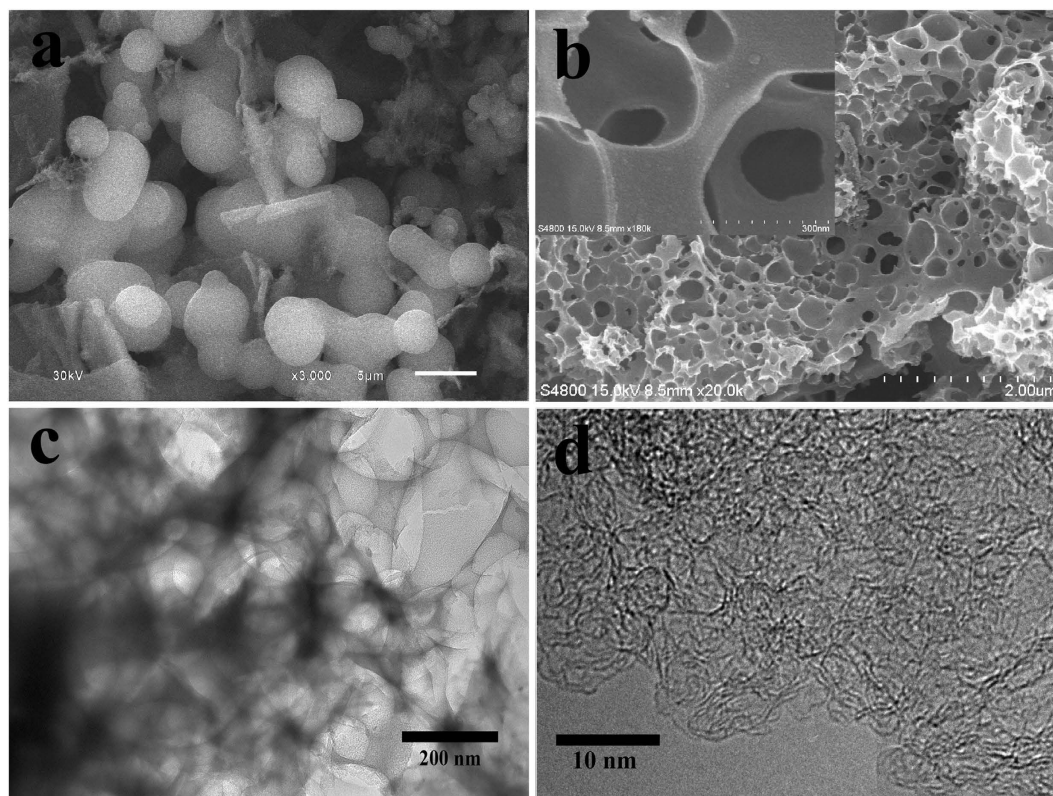


**Figure 1.** SEM images of biochar (a) and the PC-800 (b). (c,d) TEM images of the PC-800 at different magnifications.

with potential to create significant economic valorisation, is highly desired. Herein we employ stem bark with complex multilayered structure from *broussonetia papyrifera* (BP) as the carbon precursor to develop a simple and facile method for the large-scale production of nitrogen doped ACs.

It is well known that BP is a species of flowering plant in the family moraceae. Importantly, the initial oxygen and nitrogen contents of the stem bark from BP are around 50 wt% and 1.5 wt%, respectively<sup>16–19</sup>. Therefore, the BP stem bark should be a promising carbon precursor for the production of heteroatom-doped ACs due to its cheap, abundant, and a sustainable biological resource. In the present study, we prepared hetero-oxygen (9.09%) and -nitrogen (1.7%) co-doped porous carbon with a high BET surface area via hydrothermal treatment of stem bark with complex multilayered structure from BP as the biomass precursor, and following thermal activation by KOH at 800 °C. The applications of this novel heteroatom doped porous carbon in high-power supercapacitors and CO<sub>2</sub> capture are also demonstrated.

## Results and Discussion

**Synthesis and Characterization of Nitrogen Doped Porous Carbon.** As mentioned previously, heteroatom doped porous carbon with high BET surface area was prepared via a two-step progress, in which the BP stem bark was first hydrothermal treated in 1 M diluted sulfuric acid and then thermal activated by KOH at 700–900 °C. The resultant carbon materials are denoted as PC-700, PC-800, and PC-900, respectively. In the first step of hydrothermal treatment, the BP stem barks undergo acid-catalyzed dehydration, fragmentation, rearrangement and polymerization reactions to produce acid-insoluble intermediate biochar including spherical conjugated aromatic carbonaceous materials<sup>20–22</sup> and pseudo-lignin, which consists of carbonyl, carboxylic, aromatic and aliphatic structures. Usually, spherical structure with diameter of 2–5 μm and flake from residual BP stem bark can be observed, which is consistent with our SEM observations (see Fig. 1a). Then during thermal activation at high temperature, the KOH activation involves primary reaction of  $6\text{KOH} + 2\text{C} = 2\text{K} + 3\text{H}_2 + 2\text{K}_2\text{CO}_3$ , decomposition of  $\text{K}_2\text{CO}_3$  to  $\text{K}_2\text{O}$ , and reactions of  $\text{K}/\text{K}_2\text{O}/\text{K}_2\text{CO}_3/\text{CO}_2$  with carbon<sup>23,24</sup>. In addition, the abundant oxygen functional groups in biochar can react with KOH during heating, and generate H<sub>2</sub>O and CO<sub>2</sub> gases because of dehydration and decarboxylation<sup>24</sup>. Particularly, upon heating to high temperature, the biochar undergo much stronger dehydrogenation and intermolecular dehydration reactions. As a result, serious structural changes are induced, leading to a much more porous network in final products. Considering the fact that the synthesis parameters, such as the hydrothermal temperature, H<sub>2</sub>SO<sub>4</sub> concentration, biochar/KOH mass ratio, and activation temperature, play important roles in the regulation of the capacitance performance of the final porous carbons, a series of experiments were performed in order to screen the optimal synthesis conditions. Our experimental results confirm that the optimal synthesis conditions are: hydrothermal temperature = 170 °C, H<sub>2</sub>SO<sub>4</sub> concentration = 1 M, biochar/KOH mass ratio = 1/2, and activation temperature = 700 ~ 900 °C (see Supporting

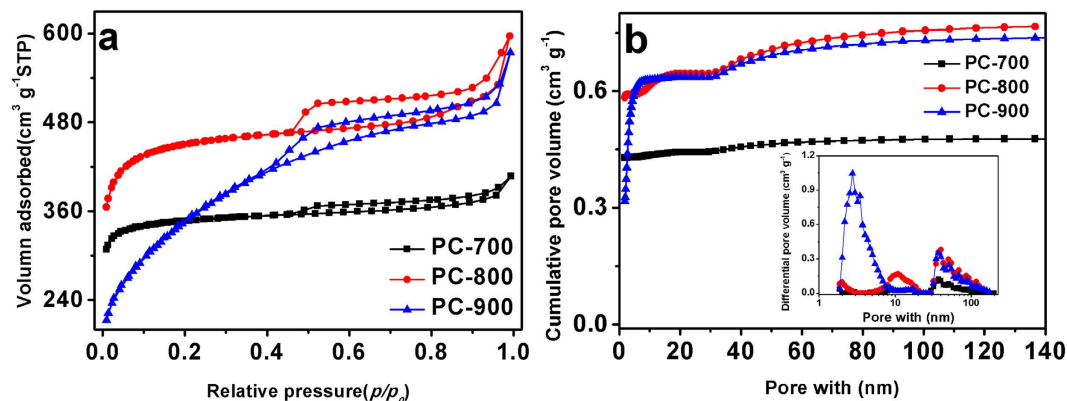


**Figure 2.**  $N_2$  adsorption-desorption isotherms (a) and pore size distributions (b) of the PC-700, PC-800, and PC-900.

Sample	BET SSA ( $m^2 g^{-1}$ )				Pore volume ( $cm^3 g^{-1}$ )				Pore width (nm)	$C_g^c$ ( $F g^{-1}$ )	$CO_2^d$ Adsorption ( $mmol g^{-1}$ )
	Total	Micro	External	Ratio <sup>a</sup>	Total	Micro	External	Ratio <sup>b</sup>			
PC-700	1393	1282	111	11.55	0.63	0.49	0.14	3.50	3.17	314	3.92
PC-800	1759	1539	220	7.00	0.92	0.60	0.32	1.88	3.11	416	4.45
PC-900	1229	350	879	0.40	0.89	0.15	0.74	0.20	2.79	252	3.76

**Table 1.** Textural electrochemical and  $CO_2$  adsorption properties of the PCs. <sup>a</sup>The micropore area to external area ratio. <sup>b</sup>The micropore volume to external volume ratio. <sup>c</sup>The  $C_g$  values calculated from GC curves at a current density of  $0.5 A g^{-1}$ , see Fig. 5c. <sup>d</sup>The  $CO_2$  adsorption capacities measured under ambient pressure at  $25^\circ C$ .

Information, Figs S2 and S3 and Tables S1 and S2). Figure 1b shows the SEM image of the resultant PC-800, demonstrating that the prepared porous carbon sample possesses a continuous branched porous framework consisted of carbon nanosheets and fully interconnected pores ranges from several to hundreds of nanometers (Fig. 1b and the inset). The porous sheet-like structure is further studied by TEM observation. The typical TEM image (see Fig. 1c) reveals that the PC-800 has obvious porous texture. In addition, the localized graphitic structure which leads to an enhanced conductivity, can be seen from high-resolution TEM image in Fig. 1d.

The textural structure of the obtained porous carbons is investigated by  $N_2$  adsorption at  $77.3 K$ . As shown in Fig. 2a, the isotherms of PCs exhibit a typical type-IV curve with an obvious type-H4 hysteresis loop at  $p/p_0 = 0.45$ . The existence of type-H4 hysteresis loop is indicative of the presence of large mesopores embedded in a matrix with interconnected channels of much smaller size<sup>25,26</sup>. Figure 2b shows the pore size distribution (PSD) of the samples at different activation temperatures calculated according to NLDFT model. The meso and macro-pores increase with the temperature increment. The textural and electrochemical properties of these samples are summarized in Table 1 in detail. The PC-800 exhibits the BET surface of  $1759 m^2 g^{-1}$ , which is much higher than that of PC-700 ( $1393 m^2 g^{-1}$ ) and PC-900 ( $1229 m^2 g^{-1}$ ) as well as the highest pore volume of  $0.92 m^3 g^{-1}$ .

The XRD patterns of the obtained PC samples at 700, 800 and 900 °C are shown in Fig. 3a. All samples show two weak diffraction peaks centered at  $2\theta = 23.2^\circ$  and  $43^\circ$ , respectively. The value of  $d_{002}$  is about 0.38 nm, larger than that of graphite (0.335 nm), implying a random combination of graphitic and turbostratic stacking<sup>27,28</sup>. In addition, with increasing calcination temperature, the intensities of the  $2\theta$  peaks at approximately  $43^\circ C$  increases, due to the formation of higher degree of graphitic structure at higher carbonization temperature, which will greatly improve the electrical conductivity<sup>29-31</sup>. Figure 3b is the corresponding Raman spectra, exhibiting two bands at around  $1339 cm^{-1}$  (D band) and  $1582 cm^{-1}$  (G band) for all samples. The D band is related to the presence of disordered carbon structures, while the G band is associated with the vibration of  $sp^2$ -hybridized carbon atoms in a graphitic layer<sup>32,33</sup>. The intensity ratio of D and G bands ( $I_D/I_G$ ) is known to be an indicator of the degree of graphitization, and the smaller the  $I_D/I_G$  ratio, the higher the degree of graphitization. Here, the  $I_D/I_G$  peak ratio of PC-700, PC-800, and PC-900 are determined to be 0.93, 0.90, and 0.86, respectively. The results are consistent with those from XRD patterns.

XPS measurements were further used to analyze the components and chemical bonding at the surface of the BP-derived porous carbons. As shown in Fig. 4a, all samples exhibit a predominant C 1s peak at 285 eV, a weak N 1s peak at ca. 401 eV, and an O 1s peak at ca. 533 eV. Table S3 provides the C, O, and N contents obtained from XPS analysis. The N contents are found to be 1.66, 1.43, and 0.99 atom% for the PC-700, PC-800 and PC-900, respectively, while the O contents are 10.91, 9.09, and 6.42 atom%. Clearly, the N and O contents of the prepared samples are dependent on the activation temperature. The high resolution XPS spectra of N 1s for PC-700, PC-800 and PC-900 (see Fig. 4b-d) reveal the presence of four types of N configurations. The peaks at 398.5, 400.1, and 401.1 eV indicate the N doping in the form of pyridinic-N, pyrrolic-N, and quaternary-N<sup>30,34</sup>,

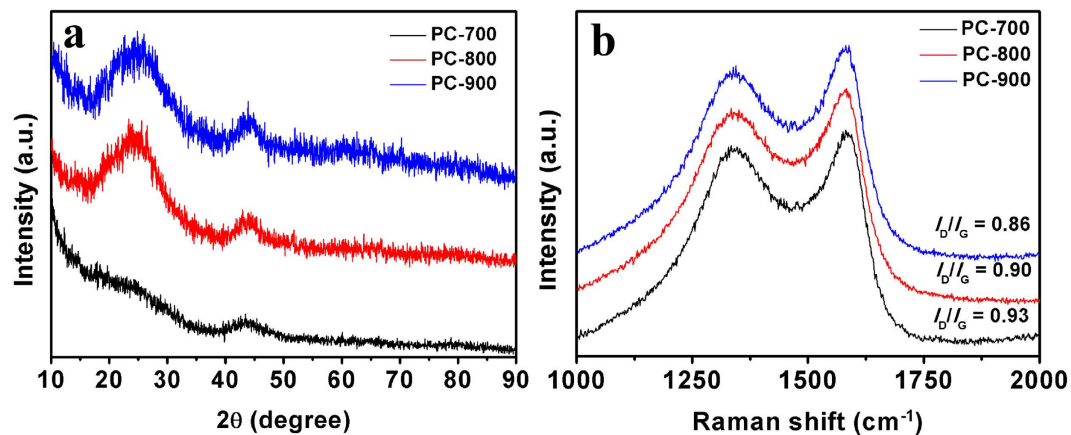


**Figure 3.** XRD patterns (a) and Raman spectra (b) of the PC-700, PC-800 and PC-900.

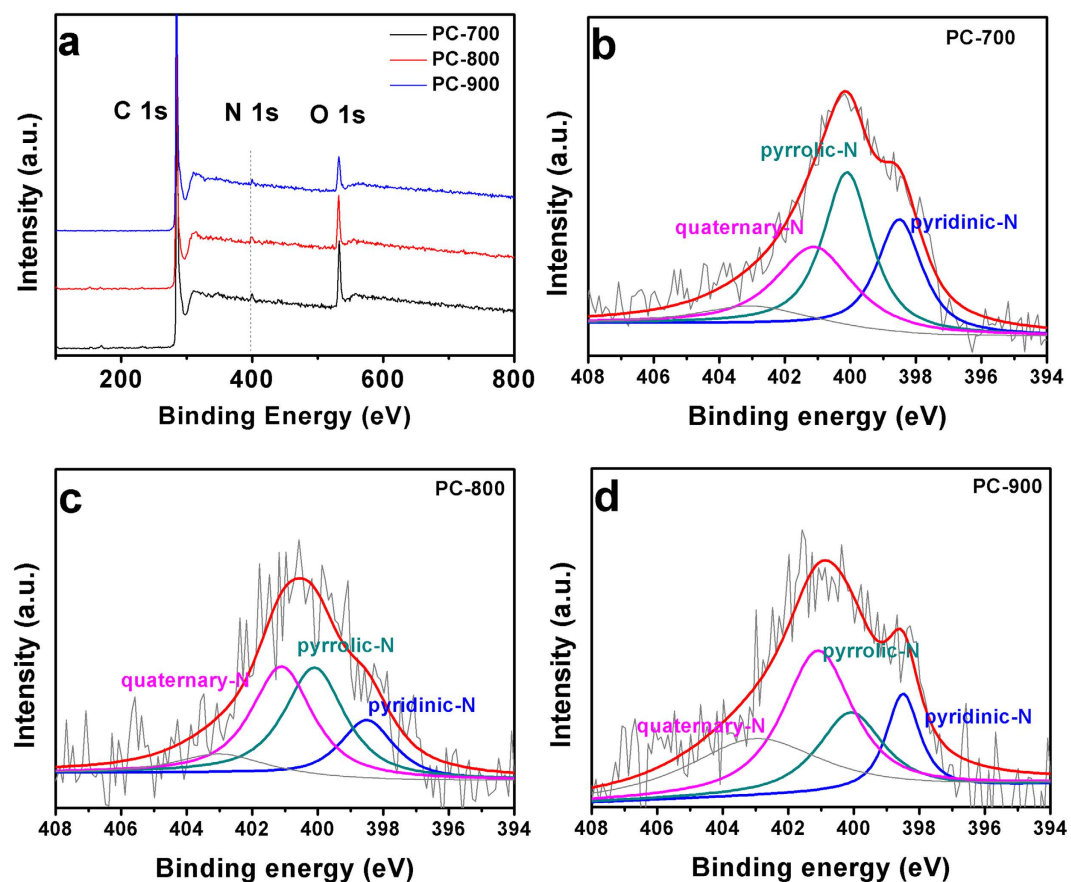


**Figure 4.** XPS survey spectra (a) and High-resolution XPS spectrum of N1s peaks (b–d) of the PC-700, PC-800, and PC-900.

respectively. As reported previously, electrochemical performance of carbons can be further enhanced by surface functionalities of O and N) due to additional pseudocapacitance<sup>35–37</sup>.

**Capacitance of the BP-Derived PCs.** Electrochemical performance of BP-derived PCs as electrode materials for supercapacitors was initially estimated using a standard three-electrode system in 6M KOH solution. The typical CV curves of the BP-derived PCs at a scan rate of 5 mV s<sup>-1</sup> and 100 mV s<sup>-1</sup> in the potential range between -1 and 0 V (vs. Hg/HgO) are shown in Fig. 5a,b. No matter at a lower scan rate of 5 mV s<sup>-1</sup> (see Fig. 5a) or a higher scan rate of 100 mV s<sup>-1</sup> (see Fig. 5b) all PCs electrodes show a quasi-rectangular shape in the CV curves, suggesting an ideal electric double-layer capacitance behavior based on ionic adsorption and exchange. On the other hand, at a higher scan rate of 100 mV s<sup>-1</sup>, no dramatic change of the CV curves is observed. The



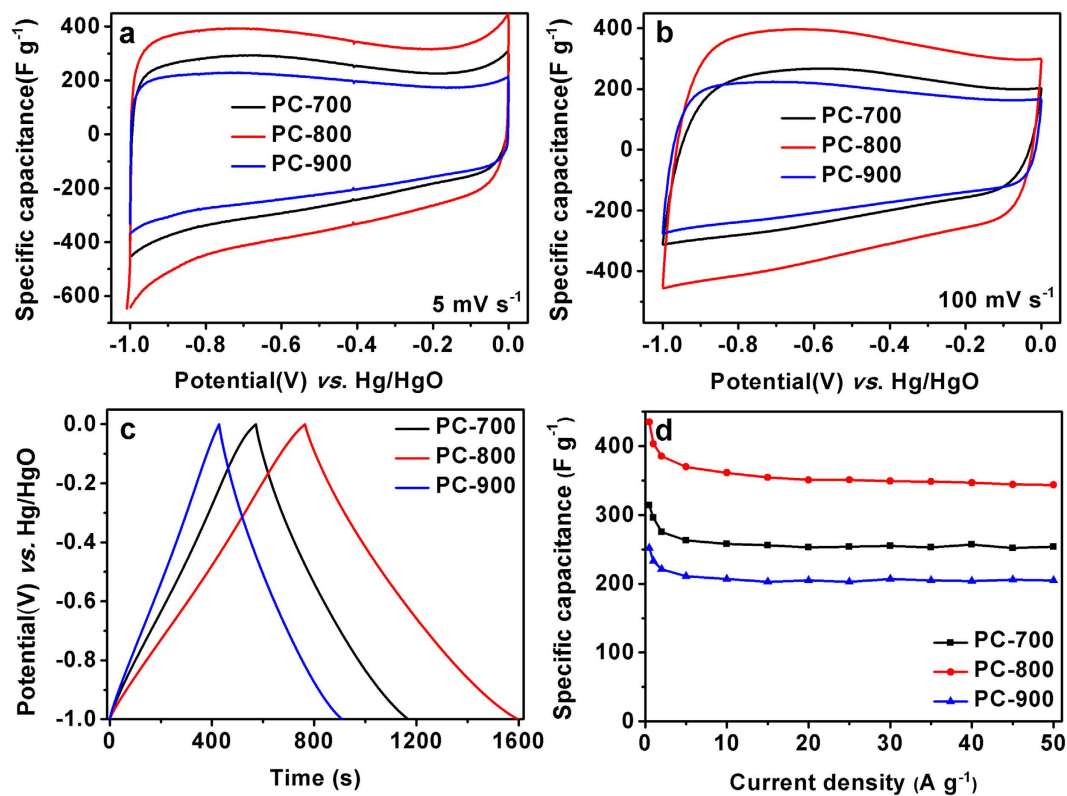


**Figure 5.** CV curves tested at a scan rate of 5 mV s<sup>-1</sup> (a) and 100 mV s<sup>-1</sup> (b), the GC curves tested at a current density of 0.5 A g<sup>-1</sup> (c), the correlation of specific capacitances with current densities (d) of the PC-700, PC-800, and PC-900.

GCD curves of these PCs electrodes are linear and display an isosceles triangle shape (Fig. 5c), indicating that the BP-derived PCs in KOH solution demonstrate ideal charge and discharge characteristics for electric double-layer capacitor. Figure 5d summarizes the gravimetric specific capacitance of three samples according to the GCD testing. It is found that the PC-800 electrode has the highest capacitance at the same current density. For instance, it possesses a specific capacitance of about 416 F g<sup>-1</sup> at 0.5 A g<sup>-1</sup>, which is higher than those from the PC-700 and PC-900 electrodes. Moreover, the capacitance of the PC-800 electrode shows only a slight decrease to 333 F g<sup>-1</sup> when the current density increased to 50 A g<sup>-1</sup>, suggesting good rate capability. Notably, the specific capacitance value of 416 F g<sup>-1</sup>, is higher than the reported values in aqueous electrolyte<sup>38,39</sup>. In addition, the PC-800 electrode shows better supercapacitor performance compared to electrodes made from various other carbon-based materials using other biomass as reported in the literatures<sup>38,40,41</sup>. The superior specific capacitance of the PC-800 electrode is ascribed to its high specific surface area, hierarchical porous structures, good conductivity, and heteroatom-doping. Considering that the rate capability is an important factor for the use of supercapacitors in power applications. The CV tests at different scan rates and GCD tests at different current densities were performed. As shown in Fig. 6c, with the scan rate increasing from 5 to 400 mV s<sup>-1</sup>, the CV curves of the PC-800 electrode become somewhat distorted but still retain a rectangular-like shape, suggesting an excellent high-rate capacitive behavior. Similarly, the GCD curves of the PC-800 electrode display a nearly isosceles triangle shape at different current densities (see Fig. 6a,b). More importantly, the GCD curves still maintain triangle shapes at a high current density of 50 A g<sup>-1</sup>, implying good coulombic efficiency (93%) and ideal capacitive behavior. The rate capability and cycling performance of the BP-derived PC electrodes based supercapacitor were further tested with a two-electrode system. The CV tested at different scan rates of 10 ~ 1000 mV s<sup>-1</sup> and GCD tested at 0.05 ~ 2 A g<sup>-1</sup> were utilized to examine the rate capability of the PC-800 based supercapacitor. As shown in Fig. 7a,b, the CV curves possess a typical rectangular shape at relative low scan rates. With increasing scan rate up to 1000 mV s<sup>-1</sup>, the CV curve still exhibits rectangular shape with only a little distortion, indicating an ideal electrochemical capacitive behavior with rapid diffusion and easy transportation of electrolyte ions to the interface of the electrode<sup>42</sup>. Figure 7c shows the GCD curves of the PC-800 supercapacitor. Clearly, the curve of 2 A g<sup>-1</sup> still maintains linear and no obvious IR drop appears, suggesting characteristics of a little internal resistance and high rate capability of the PC-800 based supercapacitor. The cycling stability of the PCs based supercapacitor during the charge-discharge process is considered as another crucial factor in practical applications. As shown in Fig. 7d, the PC-800 based supercapacitor exhibits high capacitance retention of about 87.2% after 20000 charge-discharge cycles in a two-electrode configuration at 2 A g<sup>-1</sup>, indicating excellent electrochemical cycling stability.

**CO<sub>2</sub> adsorption properties of the BP-Derived PCs.** The CO<sub>2</sub> adsorption on BP-Derived PCs was investigated at 25 and 0 °C under atmospheric pressure (1000 mbar). The CO<sub>2</sub> adsorption isotherms measured at

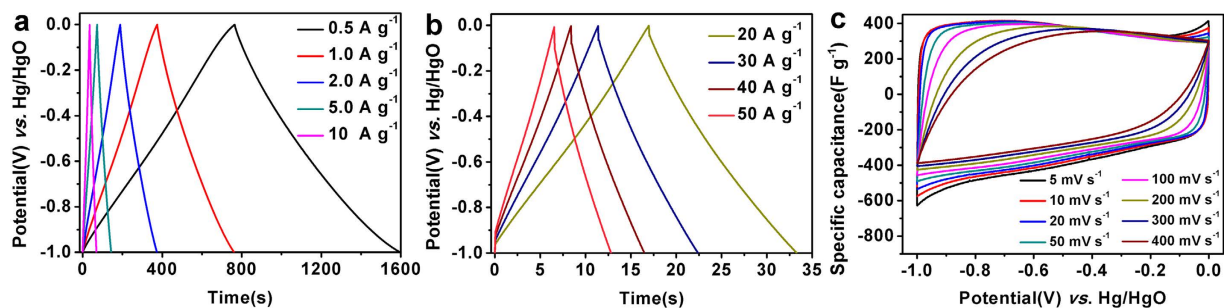


**Figure 6.** GC curves tested at 0.5–20  $A g^{-1}$  (a,b) and the CV curves tested at scan rates of 5–400  $mV s^{-1}$  (c) of the PC-800 electrode.

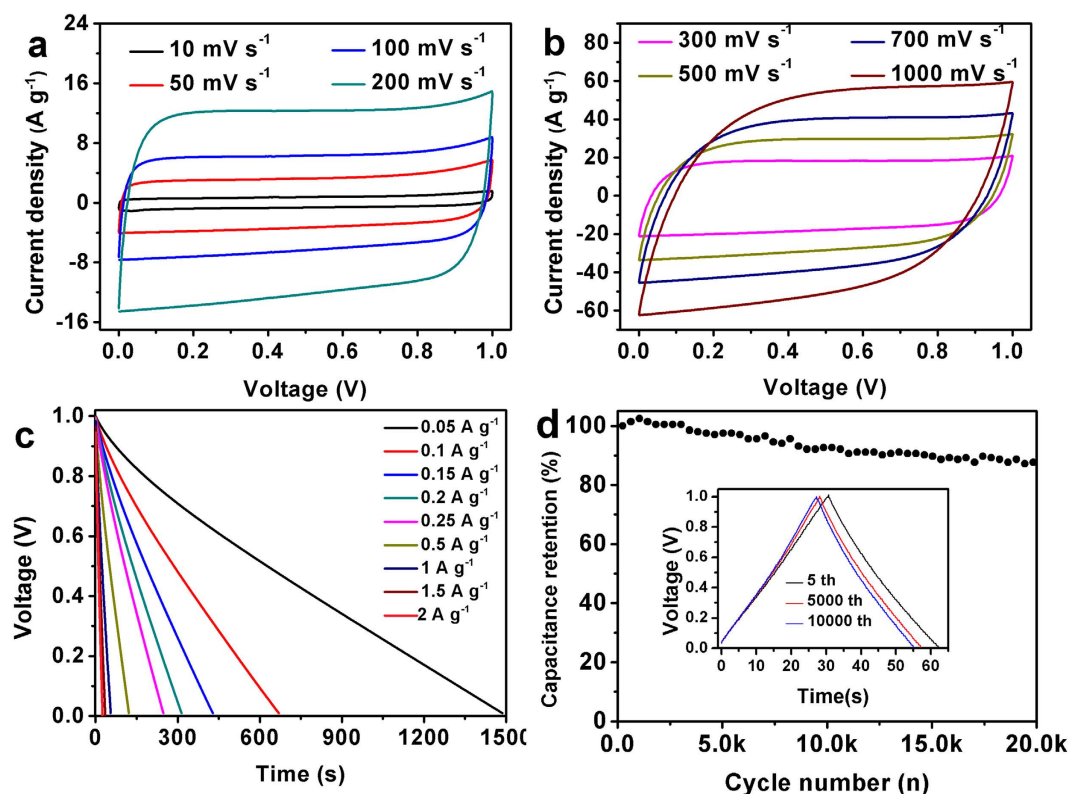


**Figure 7.** CV curves at 10–1000  $mV s^{-1}$  (a,b), GC discharge curves of 0.05–2  $A g^{-1}$  (c) and cycling performance (d) of the PC-800 based supercapacitor.

ambient conditions for all BP-Derived PCs are presented in Fig. 8. The  $CO_2$  adsorption capacities for the PC-700, PC-800 and PC-900 are about 1.06, 1.08 and 0.85  $mmol g^{-1}$  at 100 mbar, respectively (Fig. 8a). The results suggest that at very low pressure, the  $CO_2$  adsorption capacity of the porous carbons are highly depend on their nitrogen content (1.61%, 1.43% and 0.99% shown in Table S3)<sup>11,19</sup>. When the pressure increases to 1000 mbar, the  $CO_2$  adsorption capacities increase to 3.91, 4.45 and 3.76  $mmol g^{-1}$ , respectively, for the PC-700, PC-800 and PC-900, which is consistent with the BET results in Table 1. Particularly, the PC-800 has the unprecedented  $CO_2$  adsorption capacities of 4.45 and 6.71  $mmol g^{-1}$  at 25 and 0 °C, respectively, which are higher than those of the reported carbons and comparable to the nitrogen containing carbons<sup>19,31,43</sup>. For example, the activated polypyrrole showed the  $CO_2$  uptake only of 6.2  $mmol g^{-1}$  at 0 °C<sup>44,45</sup> and active poplar anthers had the  $CO_2$  uptake only of 4.18  $mmol g^{-1}$  at 25 °C<sup>19</sup>. It should be pointed that the  $N_2$  adsorption capacities for the PC-800 under ambient pressure at 0 °C is only 0.48  $mmol g^{-1}$  (7.1% of  $CO_2$  adsorption capacities). Therefore, the PC-800 with even minor nitrogen doping, is still a potential selective adsorbent for  $CO_2$  and  $N_2$  separation. Figure 8d shows the  $CO_2$  adsorption capacities at 0 °C for the PC-800 from 0 to 1000 mbar with seven repeated runs. Clearly, the adsorption amounts for the PC-800 keep almost unchanged at 0 °C in the measured pressure ranges within seven runs, demonstrating its high recyclable stability for capture of  $CO_2$ .

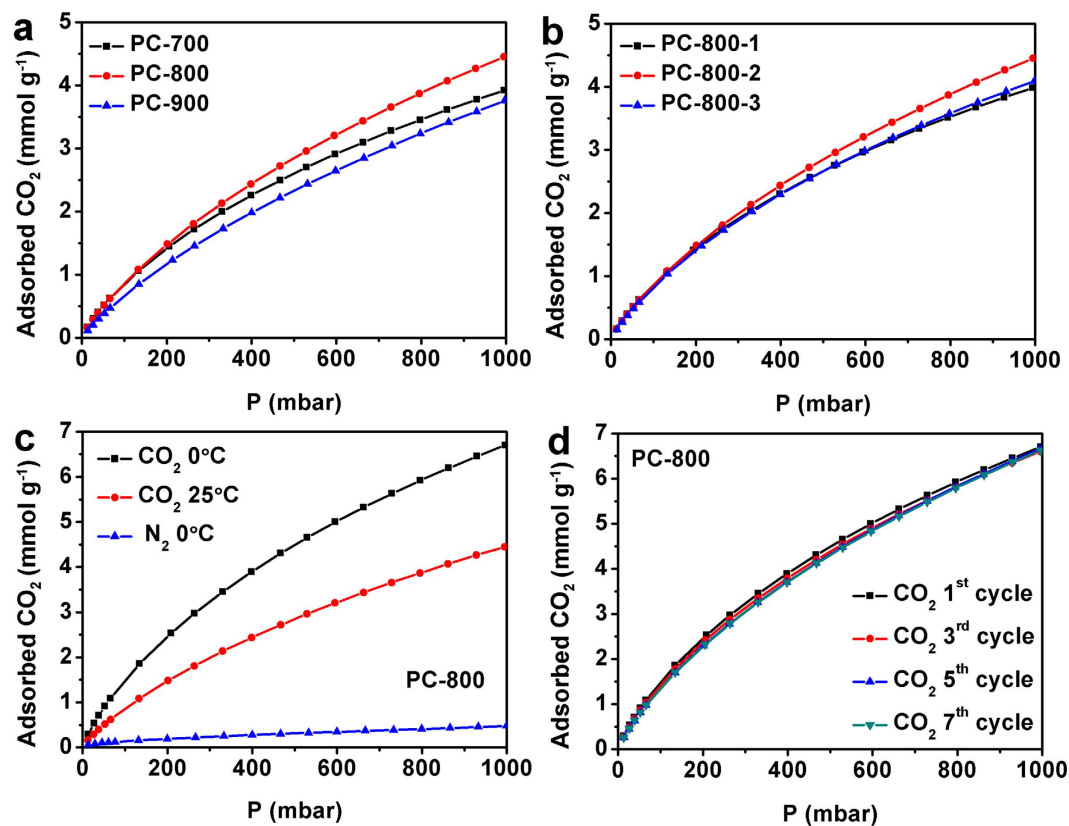


**Figure 8.** CO<sub>2</sub> adsorption isotherms (a,b) on different porous carbons at 25 °C and 0–1000 mbar, (c) CO<sub>2</sub> adsorption isotherms and N<sub>2</sub> adsorption isotherms on the PC-800 and (d) CO<sub>2</sub> adsorption isotherms on the PC-800 at 0 °C and 0–1000 mbar within seven repeated cycles with regeneration.

## Conclusions

In summary, hetero-oxygen and nitrogen doped porous carbons have been produced via hydrothermal treatment of stem bark with complex multilayered structure from BP as the biomass precursor in diluted sulfuric acid, and following thermal activation by KOH at 800 °C. The as-synthesized hetero-atom porous carbon possesses a partial graphitic structure with a very high specific surface area of 1759 m<sup>2</sup> g<sup>-1</sup> and a high pore volume of 0.92 cm<sup>3</sup> g<sup>-1</sup>. The hetero-atom doped PCs based electrode for supercapacitor displays a high specific capacitance of 416 F g<sup>-1</sup> at 0.5 A g<sup>-1</sup>, together with superior rate capability and cycling stability. As a solid-state adsorbent, the hetero-atom doped PCs has an excellent CO<sub>2</sub> adsorption capacity at ambient pressures of up to 6.71 and 4.45 mmol g<sup>-1</sup> at 0 and 25 °C, respectively. Considering the worldwide abundance and recyclability of BP, its stem bark can be acted as a novel biomass source for large-scale production of the PCs for high-performance supercapacitors and CO<sub>2</sub> adsorbent.

## Experimental

**Materials.** BP stem bark was collected from a local plantation and was prior washed, cut into pieces (1 cm × 1 cm) and dried. All of the other chemicals were analytical grade and were purchased from Aladdin Reagent (Shanghai) Co., Ltd. without further treatment.

**Preparation of Nitrogen Doped Porous Carbon.** Nitrogen doped porous carbon were prepared by carbonization and activation of the hydrothermal product of BP stem bark. Detailed procedures are as follows: 10.0 g of BP stem bark and 200 mL of 1 M diluted sulfuric acid were placed in a 250 mL stainless steel autoclave. The autoclave was sealed and heated at 170 °C for 10 h and then allowed to cool to room temperature. The resulting carbonaceous solid, denoted as biochar, was recovered by filtration, washed with distilled water, and dried. The biochar material was chemically activated using potassium hydroxide. The biochar and KOH were thoroughly ground in an agate mortar in a 1:2 mass ratio, and then the mixture was heated at 700–900 °C (5 °C min<sup>-1</sup>) for 1 h under argon flow. After that, the activated samples were thoroughly washed with 10 wt % HCl and distilled water. Finally, the carbons were dried in an oven at 100 °C for 12 h.

**Structural Characterization.** The morphology of the obtained porous carbons was characterized by scanning electron microscopy (SEM, JEOL JSM-6610LV and JEOL S-4800) operated at an acceleration voltage of 10 kV. Transmission electron microscopy (TEM) images were obtained using a JEOL JEM-1011 microscope operating at 200 kV. High-resolution TEM (HRTEM) was performed using a JEM-2100 F microscope operating at an accelerating voltage of 200 kV. The crystallographic information of porous carbons was investigated by powder

X-ray diffraction (XRD, Rigaku D/Max 2500PC). Raman spectra were collected on a Renishaw inVia Raman spectrometer. X-ray photoelectron spectroscopy (XPS) was performed on a 1063 photoelectron spectrometer (Thermo Fisher Scientific, England) with Al-K $\alpha$  X-ray radiation as the X-ray source for excitation. The textural properties were characterized by N<sub>2</sub> sorption measurements at 77.3 K (Micromeritics TriStar II 3020). The specific surface area was obtained by Brunauer-Emmett-Teller (BET) method. The pore size distribution (PSD) was calculated by the nonlocal density functional theory (NLDFT) method. The total pore volume ( $V_{\text{total}}$ ) was estimated from the adsorbed amount at a relative pressure  $p/p^\circ$  of 0.99. Micropore volume ( $V_{\text{mic}}$ ) was calculated using the t-plot method.

**Electrode Preparation and Electrochemical Measurements.** The working electrodes were typically fabricated by mixing the porous carbon as the active material (80 wt%), acetylene black (62 m<sup>2</sup>/g, 10 wt%), and polytetrafluoroethylene (PTFE, 10 wt%) in ethanol and then coated onto the nickel foam current collectors (1 cm × 1 cm) with a spatula. The premade electrodes were pressed under a pressure of 10 MPa for 5 min and finally dried at 130 °C for 12 h in an oven. The symmetric two-electrode supercapacitor was assembled into a total of 2032 stainless steel coin cells in air with nearly identical (both weight and size) electrodes, the electrolyte (6 M KOH) and a glassy fibrous separator.

The capacitive performance of single electrode was studied on a CHI760D electrochemical workstation (CH Instruments Inc., Shanghai, China) using a standard three-electrode system with platinum wire and Hg/HgO electrode as counter and reference electrodes, respectively, in 6 M KOH electrolyte at 25 °C. Cyclic voltammetry (CV), galvanostatic charge-discharge (GCD) technique and alternating current impedance were employed in the electrochemical investigations. CV tests of individual electrode were carried out between −1.0 and 0 V (vs. Hg/HgO). GC tests were performed at different current density varying from 0.5 to 50 A g<sup>−1</sup> in the same potential range as the CV test. The specific capacitance based on GC was calculated using the equation<sup>17,18</sup>:  $C_g = I/(mdV/dt)$ , where  $I$  is the constant current and  $m$  the mass of active materials, and  $dV/dt$  is calculated from the slope obtained by fitting a straight line to the discharge curve from the end of the voltage drop to the end of the discharge process. Gravimetric capacitance from GC of the two two-electrode configuration was calculated by using the formula  $C_g = 4I/(mdV/dt)$ .

**CO<sub>2</sub> Capture Measurements.** The CO<sub>2</sub> adsorption isotherms of the samples were measured using a Micromeritics TriStar II 3020 static volumetric analyzer at 0 and 25 °C. The N<sub>2</sub> adsorption isotherms of the BP-800 were measured using a Micromeritics TriStar II 3020 static volumetric analyzer at 0 °C. Prior to each adsorption experiment, the sample was degassed for 10 h at 150 °C to ensure that the residual pressure was below  $1 \times 10^{-3}$  mbar. After the samples were cooled down to 0 or 25 °C, CO<sub>2</sub> was introduced into the system. The CO<sub>2</sub> adsorption capacity in terms of the adsorbed volume under standard temperature and pressure was then recorded. The recycling adsorption test of CO<sub>2</sub> was performed with a simple regeneration by evacuating at 150 °C for 10 h under a pressure of  $1 \times 10^{-3}$  mbar<sup>19</sup>.

## References

- Sevilla, M. & Mokaya, R. Energy storage applications of activated carbons: supercapacitors and hydrogen storage. *Energy Environ. Sci.* **7**, 1250–1280 (2014).
- Lillo-Ródenas, M., Cazorla-Amorós, D. & Linares-Solano, A. Understanding chemical reactions between carbons and NaOH and KOH: an insight into the chemical activation mechanism. *Carbon* **41**, 267–275 (2003).
- Molina-Sabio, M., Rodríguez-Reinoso, F., Caturla, F. & Selles, M. Porosity in granular carbons activated with phosphoric acid. *Carbon* **33**, 1105–1113 (1995).
- Tsai, W., Chang, C. & Lee, S. A low cost adsorbent from agricultural waste corn cob by zinc chloride activation. *Bioresour. Technol.* **64**, 211–217 (1998).
- Wang, R. *et al.* Nitrogen-rich mesoporous carbon derived from melamine with high electrocatalytic performance for oxygen reduction reaction. *J. Power Sources* **261**, 238–244 (2014).
- Hao, P. *et al.* Graphene-based nitrogen self-doped hierarchical porous carbon aerogels derived from chitosan for high performance supercapacitors. *Nano Energy* **15**, 9–23 (2015).
- Guo, D.-C. *et al.* Ionic liquid C16mimBF<sub>4</sub> assisted synthesis of poly (benzoxazine-co-resol)-based hierarchically porous carbons with superior performance in supercapacitors. *Energy Environ. Sci.* **6**, 652–659 (2013).
- Wei, J. *et al.* Controllable synthesis of rich nitrogen-doped ordered mesoporous carbon for CO<sub>2</sub> capture and supercapacitors. *Adv. Funct. Mater.* **23**, 2322–2328 (2013).
- Liu, X. *et al.* Biomass-derived nitrogen self-doped porous carbon as effective metal-free catalysts for oxygen reduction reaction. *Nanoscale* **7**, 6136–6142 (2015).
- Wang, H. *et al.* Interconnected carbon nanosheets derived from hemp for ultrafast supercapacitors with high energy. *ACS nano* **7**, 5131–5141 (2013).
- Xing, W. *et al.* Superior CO<sub>2</sub> uptake of N-doped activated carbon through hydrogen-bonding interaction. *Energy Environ. Sci.* **5**, 7323–7327 (2012).
- Rufford, T. E., Hulicova-Jurcakova, D., Zhu, Z. & Lu, G. Q. Nanoporous carbon electrode from waste coffee beans for high performance supercapacitors. *Electrochem. Commun.* **10**, 1594–1597 (2008).
- Pintor, M.-J. *et al.* Preparation of activated carbon from *Turbinaria turbinata* seaweeds and its use as supercapacitor electrode materials. *C. R. Chim.* **16**, 73–79 (2013).
- Wei, L. *et al.* Hydrothermal carbonization of abundant renewable natural organic chemicals for high-performance supercapacitor electrodes. *Adv. Energy Mater.* **1**, 356–361 (2011).
- Yan, J., Wang, Q., Wei, T. & Fan, Z. Recent Advances in Design and Fabrication of Electrochemical Supercapacitors with High Energy Densities. *Adv. Energy Mater.* **4**, 1–41 (2013).
- Xi, D., Li, J., Kuang, Y.-w., Xu, Y.-m. & Zhu, X.-m. Influence of traffic exhausts on elements and polycyclic aromatic hydrocarbons in leaves of medicinal plant *Broussonetia papyrifera*. *Atmos. Pollut. Res.* **4**, 370–376 (2013).
- Zhu, Y. *et al.* Carbon-based supercapacitors produced by activation of graphene. *Science* **332**, 1537–1541 (2011).
- Wang, R. *et al.* Promising porous carbon derived from celuce leaves with outstanding supercapacitance and CO<sub>2</sub> capture performance. *ACS appl. mater. interfaces* **4**, 5800–5806 (2012).
- Song, J., Shen, W., Wang, J. & Fan, W. Superior carbon-based CO<sub>2</sub> adsorbents prepared from poplar anthers. *Carbon* **69**, 255–263 (2014).



20. Alatalo, S.-M. *et al.* Soy protein directed hydrothermal synthesis of porous carbon aerogels for electrocatalytic oxygen reduction. *Carbon* **96**, 622–630 (2016).
21. White, R. J., Brun, N., Budarin, V. L., Clark, J. H. & Titirici, M. M. Always look on the “light” side of life: sustainable carbon aerogels. *ChemSusChem* **7**, 670–689 (2014).
22. Antonietti, M., Fehler, N. & Feller, T.-P. Carbon aerogels and monoliths: control of porosity and nanoarchitecture via Sol–Gel routes. *Chem. Mater.* **26**, 196–210 (2014).
23. He, X. *et al.* Synthesis of hierarchical porous carbons for supercapacitors from coal tar pitch with nano-Fe<sub>2</sub>O<sub>3</sub> as template and activation agent coupled with KOH activation. *J. Mater. Chem. A* **1**, 9440–9448 (2013).
24. Zheng, X. *et al.* Oriented and Interlinked Porous Carbon Nanosheets with an Extraordinary Capacitive Performance. *Chem. of Mater.* **26**, 6896–6903 (2014).
25. Sing, K. S. Reporting physisorption data for gas/solid systems with special reference to the determination of surface area and porosity. *Pure and appl. chem.* **57**, 603–619 (1985).
26. Groen, J. C., Peffer, L. A. A. & Pérez-Ramírez, J. Pore size determination in modified micro- and mesoporous materials. Pitfalls and limitations in gas adsorption data analysis. *Microporous and Mesoporous Mater.* **60**, 1–17 (2003).
27. Sevilla, M. & Fuertes, A. B. Fabrication of porous carbon monoliths with a graphitic framework. *Carbon* **56**, 155–166 (2013).
28. Inagaki, M. *New carbons-control of structure and functions.* (Elsevier, 2000).
29. Ma, Y. *et al.* The production of carbon microtubes by the carbonization of catkins and their use in the oxygen reduction reaction. *Carbon* **49**, 5292–5297 (2011).
30. Qian, W. *et al.* Human hair-derived carbon flakes for electrochemical supercapacitors. *Energy Environ. Sci.* **7**, 379–386 (2014).
31. Yu, J. *et al.* One-pot synthesis of highly ordered nitrogen-containing mesoporous carbon with resorcinol–urea–formaldehyde resin for CO<sub>2</sub> capture. *Carbon* **69**, 502–514 (2014).
32. Ferrari, A. & Robertson, J. Resonant Raman spectroscopy of disordered, amorphous, and diamondlike carbon. *Phys. Rev. B.* **64**, 1–13 (2001).
33. Kaufman, J., Metin, S. & Saperstein, D. Symmetry breaking in nitrogen-doped amorphous carbon: Infrared observation of the Raman-active G and D bands. *Phys. Rev. B* **39**, 13053–13060 (1989).
34. Kapteijn, F., Moulijn, J., Matzner, S. & Boehm, H.-P. The development of nitrogen functionality in model chars during gasification in CO<sub>2</sub> and O<sub>2</sub>. *Carbon* **37**, 1143–1150 (1999).
35. Li, Z. *et al.* Mesoporous nitrogen-rich carbons derived from protein for ultra-high capacity battery anodes and supercapacitors. *Energy Environ. Sci.* **6**, 871–878 (2013).
36. Chandra, V. *et al.* Highly selective CO<sub>2</sub> capture on N-doped carbon produced by chemical activation of polypyrrole functionalized graphene sheets. *Chem. Commun.* **48**, 735–737 (2012).
37. Bagreev, A., Angel Menendez, J., Dukhno, I., Tarasenko, Y. & Bandosz, T. J. Bituminous coal-based activated carbons modified with nitrogen as adsorbents of hydrogen sulfide. *Carbon* **42**, 469–476 (2004).
38. Peng, C. *et al.* Promising activated carbons derived from waste tea-leaves and their application in high performance supercapacitors electrodes. *Electrochim. Acta* **87**, 401–408 (2013).
39. Jiang, L. *et al.* High rate performance activated carbons prepared from ginkgo shells for electrochemical supercapacitors. *Carbon* **56**, 146–154 (2013).
40. Li, X. *et al.* Preparation of capacitor’s electrode from sunflower seed shell. *Bioresour. technol.* **102**, 1118–1123 (2011).
41. Zhu, H., Wang, X., Yang, F. & Yang, X. Promising carbons for supercapacitors derived from fungi. *Adv. mater.* **23**, 2745–2748 (2011).
42. Wang, J. *et al.* Fabrication of porous carbon spheres for high-performance electrochemical capacitors. *RSC Adv.* **4**, 7538–7544 (2014).
43. Sha, Y. *et al.* Facile preparation of nitrogen-doped porous carbon from waste tobacco by a simple pre-treatment process and their application in electrochemical capacitor and CO<sub>2</sub> capture. *Mater. Res. Bull.* **64**, 327–332 (2015).
44. Sevilla, M., Valle-Vigón, P. & Fuertes, A. B. N-doped polypyrrole-based porous carbons for CO<sub>2</sub> capture. *Adv. Funct. Mater.* **21**, 2781–2787 (2011).
45. Xu, L. *et al.* Nitrogen-doped porous carbon spheres derived from d-glucose as highly-efficient CO<sub>2</sub> sorbents. *RSC Adv.* **5**, 37964–37969 (2015).

## Acknowledgements

Financial support from Program for NSFC (51472209, 51272219, U1401241), RFDP (20124301110006) the Research Foundation of Education Bureau of Hunan Province, China (Grant No. 15B237) and the Construct Program of the Key Discipline in Hunan Province is greatly acknowledged.

## Author Contributions

T.W., X.W. and H.L. designed the experiments and wrote the manuscript. T.W. worked on materials synthesis and characterization of morphology and composition. Q.Z. and Y.G. performed supercapacitor fabrication, galvanostatic charge-discharge measurements, and CV measurements. T.W. contributed to data analysis and analytical characterization. X.W. and H.L. managed the research team. All authors reviewed the manuscript.

## Additional Information

**Supplementary information** accompanies this paper at <http://www.nature.com/srep>

**Competing financial interests:** The authors declare no competing financial interests.

**How to cite this article:** Wei, T. *et al.* A Facile and Low-Cost Route to Heteroatom Doped Porous Carbon Derived from *Broussonetia Papyrifera* Bark with Excellent Supercapacitance and CO<sub>2</sub> Capture Performance. *Sci. Rep.* **6**, 22646; doi: 10.1038/srep22646 (2016).



This work is licensed under a Creative Commons Attribution 4.0 International License. The images or other third party material in this article are included in the article’s Creative Commons license, unless indicated otherwise in the credit line; if the material is not included under the Creative Commons license, users will need to obtain permission from the license holder to reproduce the material. To view a copy of this license, visit <http://creativecommons.org/licenses/by/4.0/>